ELSEVIER

Diffusive tortuosity factor of solid and soft cake layers:
A random walk simulation approach

Albert S. Kim*, Huaiqun Chen

Civil and Environmental Engineering, University of Hawaii at Manoa, 2540 Dole Street, Honolulu, HI 96822, USA

Abstract

Diffusive tortuosity factor of solid (colloidal) and soft (biofilm) cake layers formed during membrane filtration is investigated using the random walk simulation of solute tracers. Four different structures are investigated as possible candidate structures of the cake layers: simple cubic (SC), body-centered cubic (BCC), face-centered cubic (FCC), and random colloidal cake (RCC) structures. Low porosity of the deformable, compressible soft cake is mimicked by allowing overlaps among the adjacent particles and taking into account only the void spaces. When the volume fraction of each structure is less than its own maximum packing ratio of mono-dispersed solid spheres, Maxwell's theoretical prediction of the diffusive tortuosity factor is accurately superimposed on the simulation results, showing structural indifference of the tortuosity factor. However, when the soft cake is compressed so that the volume fraction becomes greater than the maximum packing ratio, the diffusive tortuosity factor surpasses Maxwell's theory and tends to diverge as the porosity reaches zero. The deviation of simulation results from the theory starts near the maximum packing ratio of each structure, and SC and FCC structures show higher diffusive tortuosity factors in comparison to the BCC structure. Most important, the RCC layer with a realistic irregular configuration has the highest diffusive tortuosity factor over almost the entire range of volume fraction. This implies that the solute diffusion within the soft cake layer of a random irregular structure is most hindered so that the concentration polarization and osmotic pressure of the solutes are accordingly enhanced on the membrane surface.
© 2005 Elsevier B.V. All rights reserved.

Keywords: Diffusive tortuosity; Tortuosity factor; Colloidal cake; Soft cake; Biofilm; Back-diffusion; Pearsonian random walk simulation

1. Introduction

Fouling phenomena in microfiltration (MF) and ultrafiltration (UF) have been extensively studied for the crossflow membrane filtration mode. When rigid colloidal particles are removed by MF/UF membranes, the particles quickly form a concentration polarization (CP) layer on the membrane surface and develop an initial stage of declining permeate flux [1–6]. During filtration, the concentration (i.e., volume fraction) of the colloidal particles above the membrane surface is mainly governed by the applied pressure, membrane resistance, particle size, solution ionic strength, Hamaker constant of the particles, and so forth [7–10]. Unless the interparticle interactions are highly repulsive (e.g., small particles of high zeta potential in a feed solution of low ionic strength), the particles retained between the CP layer

and the membrane surface easily form a cake layer when the volume fraction reaches a certain jamming limit. If the particles are non-interacting hard spheres, the packing ratio is typically between the random loose packing ratio of 0.60 and the random close packing ration of 0.64 [11–13]. In a quasi-steady state, the thickness of the cake layer increases with applied pressure because the corresponding permeate velocity accelerates particle transport from the bulk phase towards the membrane surface. The formed cake layer, therefore, provides much higher hydraulic resistance than that of the CP layer and causes significant permeate flux decline during the filtration processes.

The colloidal fouling mechanism in nanofiltration (NF) or reverse osmosis (RO) has quite different features from that of the MF/UF processes. In the absence of particulate matter, the main cause of flux decline in NF/RO processes is the concentration polarization of solute ions. The wall concentration of the solutes determines the effective driving force, i.e., the applied pressure minus the osmotic pressure. In the presence of colloidal particles in the feed solution of the NF/RO processes, the particles also form the CP and cake layers on the membrane sur-

faces, but the hydraulic resistances from those layers are almost negligible compared to the inherent resistance of NF/RO membranes alone. Nevertheless, the cake layer of retained particles promotes remarkable permeate flux decline due to the hindered solute back-diffusion. To diffuse from the vicinity of the membrane surface to the bulk phase, the solutes need to evade the retained particles by taking tortuous paths within the colloidal cake layer. Therefore, back-diffusion is hindered; concentration polarization is enhanced; osmotic pressure is elevated; and permeate flux is eventually suppressed to a certain extent. This phenomenon is called cake-enhanced osmotic pressure (CEOP) [14] or cake-enhanced concentration polarization (CECP) [15].

When biological particles are rejected by the pressure-driven membrane processes, they form a biological cake layer called a biofilm that results in deleterious biofouling, operationally defined as an unacceptable degree of system performance loss. The initial formation of the biofilm involves the accumulation of microorganisms (e.g., bacteria, fungi, microalgae) at a phase transition interface between the CP layer of the microorganisms and the membrane surfaces. The accumulation appears in two consecutive steps: attachment and ensuing growth. With this occurrence, biofouling of the membrane surfaces could be much more problematic than abiotic colloidal fouling or chemical precipitation because attached cells degrade the surface property of polymeric membranes, ingest nutrients continuously supplied by the feed water, and multiply in a geometric fashion. A single bacterium entering a membrane module may result in extensive biofouling if the growth rate of the sessile population is high.

Adhesion of bacteria to the membrane surface increases with filtration time due to the biosynthesis of adhesive extracellular biopolymers, which are abundantly produced and then completely envelop the attached cells in a viscous hydrated gel. The biopolymers are referred to as extracellular polymeric substances (EPS) [16–18]. EPS enhance the survival and robustness of the biofilm microorganisms by serving as a transport barrier for reactive chemicals, such as antimicrobial agents attempting to penetrate into the biofilm by convective and diffusive transport mechanisms [17,19–21]. Turbulent mixing above the membrane surfaces is also diminished by the presence of EPS, which results in enhanced concentration polarization of solutes accumulating in the viscous sublayer [22]. The biofouling is therefore highly affected by the microstructure and composition of the membrane biofilms.

In contrast to the axial shear flow experienced by biofilms on their nonporous surfaces, a noticeable proportion (10 to 15%) of the fluid containing water, nutrients, and other solutes can continuously pass through the biofilms due to the transmembrane pressure. Enough food sources are thus supplied to the microorganisms and so biofilm growth kinetics is accordingly accelerated. High transmembrane pressure either condenses or compresses microorganisms in the biofilms and generates very dense structures with minute porosity. The biofilm thickness varies from a mono- to multiple-layers of cells that are typically distributed throughout the EPS matrix [18,23]. However, the cells in certain biofilms are heterogeneously disbursed, forming a complex microstructure of fluid-filled channels, i.e., void pores [20,24]. The void and heterogeneous biofilms are still not

well understood, but their impact can be extraordinarily significant because the solutes, including nutrients as well as biocides (added for cleaning of biofouled membranes), will be trapped within the small void pores of the biofilm. Note that EPS play an important role in the chemical transport barrier. Consequently, the solute back-diffusion will be hindered, causing a similar but severe phenomenon like the CEOP or CECP [14,15].

A fundamental understanding of solute diffusion within porous media is generally of great importance. In membrane filtrations, the porous media of rejected matters can be classified into two categories: solid and soft cakes. The solid cake refers to the colloidal cake layer composed of rigid, (typically) spherical particles, and the soft cake refers to a biofilm made up of deformable, compressible microorganisms usually surrounded by EPS. In both case, the solute back-diffusion is greatly hindered by the presence of the cakes and is obviously dependent on the cake porosity and structure.

In this work, we employ four different types of porous media composed of mono-sized spheres and consider them as possible cake structures formed during the membrane filtrations. Three of the crystal structures are well-known solid-state configurations (i.e., simple cubic (SC), body-centered cubic (BCC), and face-centered cubic (FCC) structures [25,26]), and the last is a computer-simulated random colloidal cake (RCC) structure formed in a dead-end colloidal membrane filtration [9]. The low porosity of deformable soft cakes is mimicked by allowing overlap of the spheres and taking into account remaining void pore spaces. The solutes are assumed to be tracers, which are chemically inert with respect to themselves as well as surfaces of the composing spheres. Finally, the diffusive tortuosity factor, defined as the ratio of the solute diffusion coefficient in a free space to that in the porous media, is predicted as a function of the porosity and structure of the cake layers by Pearsonian random walk simulation [27]. Further extensions from the current model can include the chemical reaction of solute, biofilm growth by multiplication and size change of bacteria, and transient EPS production. These will result in a complete random walk simulation model that remains true to the solute transport within the actual colloidal cake as well as the biofilm layers.

2. Hindered solute diffusion

Solute diffusion is hindered by the presence of solid or soft deposited particles that form a porous cake layer, within which a solute should take a detoured path to diffuse towards the bulk phase. In this light, a generalization of Fick's law is of great necessity [28,29] as:

$$J = -D_0 \frac{\varepsilon}{\theta^2} \frac{\partial C}{\partial y} \tag{1}$$

where J is the diffusive solute flux, C the solute number concentration within the void space of the cake layer, y the vertical coordinate normal to the membrane surface, D_0 the diffusion coefficient in the bulk phase, and ε the porosity of the cake layer. Here, θ is the diffusive tortuosity defined as dL/dx, where dL is the mean incremental distance that a solute should travel through the cake layer, and dx is the straight distance that the

solute travels in the free space [30,31]. A definition similar to the tortuosity θ is the tortuosity factor defined as θ^2 [32]. To avoid confusion of nomenclature in this paper, we will exclusively use the tortuosity factor denoted as τ ($=\theta^2$). The tortuosity factor can be determined by direct measurement of the diffusion coefficients of a non-interactive tracer species in both the free solution and porous medium of known porosity [29]. The formation factor is defined as the tortuosity factor divided by the porosity, i.e., $f = \tau/\varepsilon$, which can be also directly obtained through electric resistivity measurements that typically take less time to be determined in comparison to the direct measurement of diffusion coefficients [28]. However, the two direct measuring methods are somewhat limited to evaluating settled, stationary porous media (e.g., marine sediments [28,30,33]). Application of those methods to a cake layer in the dynamic state of membrane filtration is, for all practical purposes, not feasible.

Using the diffusive tortuosity factor and formation factor defined above, one can rewrite Eq. (1):

$$J = -D_0 \frac{1}{f} \frac{\partial c}{\partial y} = -D_\mathrm{h} \varepsilon \frac{\partial C}{\partial y} \tag{2}$$

where $D_\mathrm{h} (=D_0/\tau)$ is the hindered diffusion coefficient of solutes in the cake layer. Then, *the formation factor f is interpreted as the ratio of the diffusive flux in the bulk phase to that in the cake layer, while the tortuosity factor is considered as the ratio of the corresponding diffusion coefficients, i.e., $\tau = D_0/D_\mathrm{h}$.*

3. Fundamental theory

Transient diffusion of tracer solutes in the void space can be described by the following equations [34]:

$$\frac{\partial C}{\partial t} = D_0 \nabla^2 C \tag{3}$$

$$C(\mathbf{r}, t = 0) = C_0(\mathbf{r}) \tag{4}$$

and

$$\hat{\mathbf{n}} \cdot \nabla C = 0 \text{ (on the particle surface)} \tag{5}$$

where $\hat{\mathbf{n}}$ is a unit vector normal to the particle surface. The *effective time-dependent diffusion coefficient D (t)* is now defined as:

$$D(t) = \frac{\langle (\mathbf{r} - \mathbf{r}')^2 \rangle}{6t} \tag{6}$$

where the mean square displacement of the tracers is given as:

$$\langle (\mathbf{r} - \mathbf{r}')^2 \rangle \equiv \frac{1}{V_\mathrm{p}} \int_{V_\mathrm{p}} d^3\mathbf{r} \int_{V_\mathrm{p}} d^3\mathbf{r}' (\mathbf{r} - \mathbf{r}')^2 G(\mathbf{r}, \mathbf{r}', t) \tag{7}$$

Here, V_p is the volume of the void space of the cake layer, and $G(\mathbf{r}, \mathbf{r}', t)$ is the diffusion propagator which can be described as the probability density of finding a random walker (i.e., a tracer solute in this study) at position $\mathbf{r}$ at time t after it was released at position $\mathbf{r}'$ at time $t = 0$. For diffusion in the bulk phase (i.e., $\varepsilon \to 1$ and $\tau \to 1$), G is given as:

$$G(\mathbf{r}, \mathbf{r}', t) = \frac{1}{(4\pi D_0 t)^{3/2}} \exp\left[-\frac{(\mathbf{r} - \mathbf{r}')^2}{4D_0 t}\right] \tag{8}$$

but, for diffusion within the cake layer (i.e., $\varepsilon < 1$ and $\tau > 1$), G will depend on the structure and the volume fraction of the cake layer. The coefficient $D (t)$ initially decreases from D_0 with respect to time t and reaches D_h after a very long time:

$$D(t) = \begin{cases} D_0 & \text{for } t \to 0 \\ D_\mathrm{h} & \text{for } t \to \infty \end{cases} \tag{9}$$

Thus one can define a dimensionless time-dependent diffusion coefficient of tracers in the cake layer as:

$$\lambda \equiv \frac{D(t)}{D_0} = \frac{2\langle (\mathbf{R} - \mathbf{R}')^2 \rangle}{N} \tag{10}$$

where N is the total number of time steps and $\mathbf{R} - \mathbf{R}'$ is the dimensionless displacement defined as:

$$\mathbf{R} - \mathbf{R}' = \frac{(\mathbf{r} - \mathbf{r}')}{\bar{l}} \tag{11}$$

Here, $\bar{l}$ is the mean free path of the random walkers, which is presumed to be identical for each walker at any time. The position of random walker i immediately after it was released at position $\mathbf{R}_0^{(i)}$ is:

$$\mathbf{R}_1^{(i)} = \mathbf{R}_0^{(i)} + \Delta\mathbf{R}_1^{(i)} \tag{12}$$

and, after k movements, is:

$$\mathbf{R}_{k+1}^{(i)} = \mathbf{R}_k^{(i)} + \Delta\mathbf{R}_{k+1}^{(i)} = \mathbf{R}_0^{(i)} + \sum_{j=1}^{k+1} \Delta\mathbf{R}_j^{(i)} \tag{13}$$

where

$$|\Delta\mathbf{R}_j^{(i)}| = \sqrt{\left(\Delta X_j^{(i)}\right)^2 + \left(\Delta Y_j^{(i)}\right)^2 + \left(\Delta Z_j^{(i)}\right)^2} = 1 \tag{14}$$

which is the intrinsic characteristic of the Pearsonian random walk simulation with $\Delta\mathbf{R}_j = (\Delta X_j, \Delta Y_j, \Delta Z_j)$ [27].

3.1. Stationary diffusion coefficient

The asymptotic behavior of the square displacement of walker i after a sufficient number of time steps N in free space is:

$$\begin{aligned} (\mathbf{R}_N^{(i)} - \mathbf{R}_0^{(i)})^2 &= \left(\sum_{j=1}^{N} \Delta\mathbf{R}_j^{(i)}\right) \cdot \left(\sum_{k=1}^{N} \Delta\mathbf{R}_k^{(i)}\right) \\ &= \sum_{j=1}^{N} \left(\Delta\mathbf{R}_j^{(i)}\right)^2 + \sum_{i \neq j}^{N} \text{cross-term} \cong \sum_{j=1}^{N}(1) + 0 \\ &= N \end{aligned} \tag{15}$$

The summation of the cross-term converges to zero because the term is composed of products of two random numbers from -1 to 1. Then, λ in free space can be calculated as:

$$\lambda_\text{free} = \frac{2}{N_\mathrm{p}} \sum_{i=1}^{N_\mathrm{p}} \left[\lim_{N \to \infty} \frac{1}{N} \langle (\mathbf{R}_N^{(i)} - \mathbf{R}_0^{(i)})^2 \rangle \right] \to 1 \tag{16}$$

where N_p is the total number of random walkers and:

$$\langle (\mathbf{R}_N^{(i)} - \mathbf{R}_0^{(i)})^2 \rangle = \frac{1}{N}\sum_{j=1}^{N}(\mathbf{R}_j^{(i)} - \mathbf{R}_0^{(i)})^2 = \frac{1}{N}\sum_{j=1}^{N}j = \frac{1}{2}(N+1) \tag{17}$$

The convergence of λ to 1 in Eq. (16) is valid only for free space, but within the cake layer λ must be smaller than 1 due to the geometrical obstacles (i.e., the particles comprising the cake layer) that hinder the random walk movements. Then, the ratio of λ in the cake layer to that in free space provides the tortuosity factor, i.e.,

$$\tau = \frac{D_0}{D_h} = \frac{\lambda_{\text{free}}}{\lambda} = \frac{1}{\lambda} \tag{18}$$

Analytical evaluation of λ_{free} of Eq. (16) does not require averaging over N_p random walkers, but actual numerical simulation becomes more efficient by implementing both the time and space averages: for example, 10^3 time steps with 10^3 walkers instead of 10^6 time steps of a single walker (see Section 4.).

3.2. Short-term diffusion coefficient

Immediately after the walkers are released at arbitrary locations in pore spaces, they do not experience the presence of geometrical obstacles, i.e., particles composing a cake layer. During this short time the time-dependent diffusion coefficient can be expanded as [35–38]:

$$\frac{D(t)}{D_0} = 1 - \frac{2}{9}\sqrt{\frac{2}{\pi}}\left(\frac{S}{V_p}\right)\sqrt{2D_0 t} + O(D_0 t) \tag{19}$$

where S is the total pore surface area exposed to the walkers. $\sqrt{2D_0 t}$ is the root-mean-square distance of a tracer in one direction, and then $S\sqrt{2D_0 t}$ is the volume of walkers that have seen the pore surface. Eq. (19) can be rewritten in terms of λ and N as:

$$\lambda(N) = 1 - \frac{2}{9}\sqrt{\frac{2}{\pi}}s_p\sqrt{N} + O(N) \tag{20}$$

where s_p is termed the dimensionless surface-to-volume ratio, defined as:

$$s_p = \frac{S\sqrt{2D_0\Delta t}}{V_p} \tag{21}$$

Here, Δt is the time required for a walker to move as much as its mean free path, $\bar{l}$. Now, the dimensionless surface-to-volume ratio, s_p, can be calculated as:

$$s_p = -\lim_{\sqrt{N}\to 0}\frac{9}{2}\sqrt{\frac{\pi}{2}}\frac{\mathrm{d}\lambda(N)}{\mathrm{d}\sqrt{N}} \tag{22}$$

which is a function of volume fraction and structure of a porous medium.

4. Simulation method

Hizi and Bergman [35] conducted a molecular diffusion study in periodic porous media composed of octahedron-like obsta-

cles. In their study, generated porous media were comprised of simple cubic configurations with different porosity from completely separated to highly overlapping obstacles, and the time-dependent effective diffusion coefficient $D(t)$ was calculated using the Bloch-type eigen functions. Trinh et al. [39] studied the effective diffusion coefficient of point-like molecules in isotropic porous media by conducting Monte Carlo simulations. Geometrical obstacles were square or circular for 2D media and cubic or spherical for 3D media. Their simulations were, however, performed in a cubic lattice grid so that a random walker jumps to one of the four nearest unoccupied sites for 2D media or one of six for 3D media at each time increment. Moreover, the small number of tracers, 100, was not sufficient to investigate the short-term diffusion behavior.

In this study, Pearsonian random walk simulations are performed with four different sphere-packing structures as shown in Fig. 1. Three crystal structures (i.e., SC, BCC, and FCC) comprised of equal-sized spheres are investigated along with the RCC structure produced by a NPT Monte Carlo simulation [9]. Sphere configuration in a unit cell of each cubic structure is shown in Fig. 1(a)–(c). In the SC unit cell of Fig. 1(a), eight spheres are located at eight corners, and each of the corner spheres contributes one-eighth of its volume to the unit cell. In the BCC unit cell of Fig. 1(b), eight corners and one center have one sphere each so that net number of spheres in a BCC unit cell is 2 ($= \frac{1}{8}\times 8 + 1$). The FCC unit cell of Fig. 1(c) has one sphere at each corner and on each surface so that corner and surface spheres contribute one-eighth and one-half of their volume to the unit cell, respectively. The net number of spheres in the FCC unit cell is therefore 4 ($= \frac{1}{8}\times 8 + \frac{1}{2}\times 6$). The maximum packing ratios of SC, BCC, and FCC are $\pi/6 (\simeq 0.524)$, $\pi\sqrt{3}/8 (\simeq 0.680)$, and $\pi\sqrt{2}/6 (\simeq 0.741)$, respectively. The RCC structure composed of 256 spherical colloids shows a volume fraction of 0.58 [9], which is close to the maximum ratio of ran-
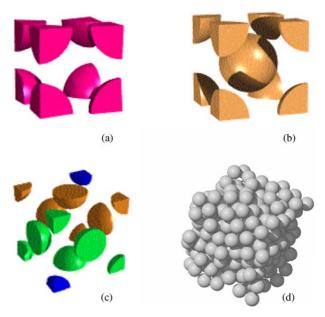

Fig. 1. Schematic diagrams of: (a) simple cubic, (b) body-centered cubic, (c) face-centered cubic, and (d) random colloidal cake structures of interacting monodispersed spheres [9].

dom loose packing (RLP) of equal-sized hard spheres [11,12]. Deformed and compressed soft cake structures are mimicked by reducing inter-particle distances at a common rate and allowing overlaps among adjacent spherical particles comprising the structures. In this case, the volume fraction of the swarm of overlapped particles is estimated by a Monte Carlo integration: a tremendous number of random positions are located in each structure, and the volume fraction is calculated as a ratio of the number of positions within void spaces to that of entire positions.

For efficient simulations, the sphere radius a is set to $100\bar{l}$ since a larger ratio of a to $\bar{l}$ did not provide any appreciable difference in a former study [34]. The periodic boundary condition is applied to the four structures to mimic the infiniteness of the porous media. The volume fraction is controlled by scaling the configuration, keeping the cake structure and sphere size unchanged. In other words, center-to-center distances among spheres are expanded/compressed to reduce/increase the volume fraction, but the relative angles among any of three spheres are not changed. During Pearsonian random walk simulations, random walker i is released from arbitrarily chosen position $\mathbf{R}_0^{(i)}$ within the void space, and it moves to next new positions of $\mathbf{R}_1^{(i)}, \mathbf{R}_2^{(i)}, \ldots, \mathbf{R}_j^{(i)}(= \mathbf{R}_{j-1}^{(i)} + \Delta \mathbf{R}_j^{(i)}), \ldots, \mathbf{R}_N^{(i)}$ consecutively as time advances. The blind reflection is applied at the surface of packed spheres: if a walker enters into a sphere, it returns to its previous position, but time advances by one step. Later the walker can diffuse away from the surface of the reflecting sphere.

To satisfy Eq. (14) of Pearsonian feature, three random numbers are generated in a sequence:

$$\delta_1 = \pm \text{rand}, \qquad \delta_2 = \pm \text{rand} \times \sqrt{1 - \delta_1^2},$$

$$\delta_3 = \pm \sqrt{1 - \delta_1^2 - \delta_2^2} \tag{23}$$

to satisfy

$$\delta_1^2 + \delta_2^2 + \delta_3^2 = 1 \tag{24}$$

where "rand" stands for a random number between 0 and 1. The displacement of walker i in each direction at time step j, $(\Delta X_j^{(i)}, \Delta Y_j^{(i)}, \Delta Z_j^{(i)})$, is arbitrarily assigned as one of six possible candidates, i.e., $(\delta_1, \delta_2, \delta_3)$, $(\delta_1, \delta_3, \delta_2)$, $(\delta_2, \delta_1, \delta_3)$, $(\delta_2, \delta_3, \delta_1)$, $(\delta_3, \delta_2, \delta_1)$, and $(\delta_3, \delta_1, \delta_2)$. This is done to avoid any possible correlation of sequentially generated random numbers, which might cause improper statistics in arbitrarily determining $\Delta X_j^{(i)}$, $\Delta Y_j^{(i)}$, and $\Delta Z_j^{(i)}$. Interestingly, we found that use of a specific order of $(\delta_1, \delta_2, \delta_3)$ caused (slightly) unequally partitioned spatial probability in the x, y, and z directions, confirming that a high-quality random number generator is very critical in statistical simulations [40].

All the simulations were performed in a parallel mode using a Beowulf Linux cluster composed of 16 PCs. Each computer has a 1.9 GHz Intel processor and 1 Giga Byte random access memory. They are connected to a data switch (NETGEAR Inc., Santa Clara, CA) through 100 mega-bits per second (MBPS) network adaptors imbedded in the motherboards. Message passing interface (MPI) [41] is harnessed for data communication among the

16 nodes (PCs) on the Linux platform of Fedora Core 1. A total of 16,000 random walkers are released into void spaces of the four structures, so each node handles 1000 walkers to generate the statistical data of mean square displacements. At every 1000 time steps, 15 slave nodes send their values of $\langle (R_N^{(i)} - R_0^{(i)})^2 \rangle$, which are less than $1/2$ $(N+1)$ of Eq. (17), to the master node. Then, the master node calculates an average of 16 data values, 15 from slave nodes and 1 from the master itself. Finally, at the end of a random walk simulation, the master node provides the diffusive tortuosity factor and formation factor of a cake layer of certain volume fraction and structure.

5. Results and discussion

5.1. Dimensionless diffusion coefficient, λ

Figs. 2–5 show transient behaviors of dimensionless diffusion coefficients of solute tracers in SC, BCC, FCC, and RCC struc-
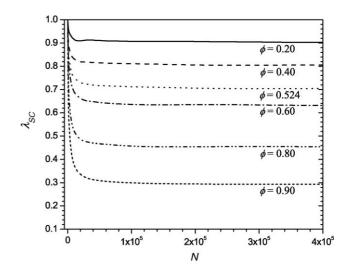

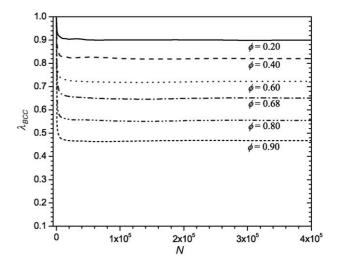Fig. 2. SC structure: dimensionless diffusion coefficient λ_{SC} as a function of time step N.

Fig. 3. BCC structure: dimensionless diffusion coefficient λ_{BCC} as a function of time step N.
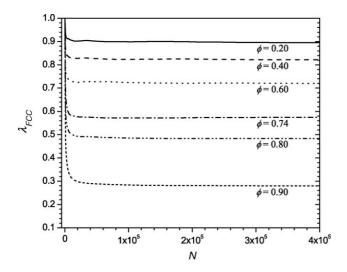
Fig. 4. FCC structure: dimensionless diffusion coefficient λ_{FCC} as a function of time step N.

tures, respectively. Each figure represents λ with volume fraction ϕ from 0.2 to 0.9 with proper intervals including the maximum packing ratio of the corresponding structure. In all cases for Figs. 2–5, λ drops significantly from 1.0 in the initial stage, slightly fluctuates afterwards, and then smoothly converges to a stable state. After the first quarter of all the simulations (i.e., $N \geq 1.0 \times 10^5$), λ does not show any noticeable transient variation, but rather stays relatively flat, rendering a steady-state self-diffusion coefficient. Consequently, the four structures provide a similar converging trend of the dimensionless diffusion coefficient λ regardless of the cake volume fraction.

It is worth noting that the configuration of the RCC structure illustrated in Fig. 1(d) has the identical converging trend of λ (shown in Fig. 5) to those of the three crystal structures. It was previously thought that the irregularity of the RCC structure could cause anomalous diffusion [40,42,43], in which the mean square displacement is not linearly proportional to the elapsed
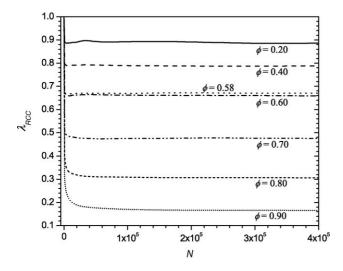
time step, i.e.,

$$\langle (\mathbf{r} - \mathbf{r}')^2 \rangle \sim t^{1-\alpha} \tag{25}$$

where the exponent α is positive. This phenomenon, however, is not detected during the simulations (see Fig. 5). The reason why the anomalous diffusion does not appear is that the "hidden" liquid-like structure of packed spheres is fully implemented by the RCC configuration, and the infiniteness of the cake layer is mimicked by the periodic boundary condition on each wall of the unit cell [9,44,45]. The random walkers therefore experience regularity in the colloidal cake layer and so perform a normal diffusion (i.e., $\alpha \to 0$) even though the colloidal cake looks irregular and random at the first glance of Fig. 1(d).

5.2. Diffusive tortuosity factor, τ

The diffusive tortuosity factor is traditionally considered as a function of a pore length (or angle) factor L' and a pore shape factor S' [46]:

$$\tau = f(L', S') \tag{26}$$

The simplest form of τ in terms of L' and S' is [47]:

$$\tau = L' S' \tag{27}$$

The factor L' takes into account the ratio of the mean distance that a tracer should detour around the geometrical obstacles to the straight distance that the tracer can travel in the free space. The shape factor S' reflects the variation of pore cross-sectional areas along pore channels. Both L' and S' are dimensionless and increase with respect to the volume fraction of porous media.

Although Armatas et al. [46] proposed a form of the length factor as:

$$L' = \frac{d_{max} - d_{min}}{d_{mean}} \tag{28}$$

where d_{max} and d_{min} are effective maximum and minimum diameters of the pore spaces, respectively, and d_{mean} is the mean pore size, to the best of our knowledge, rigorous expressions of L' and S' from a general, robust theory are not available yet. Therefore, accurate values of the tortuosity factor must be measured by careful experiments or sophisticated simulations at a fundamental level [47]. In this light, we used curves of $\lambda(N)$ versus N in Figs. 2–5 and calculated values of the tortuosity factor by employing the following relationship [35]:

$$\lambda(N) = \frac{A}{N} + \frac{1}{\tau} \tag{29}$$

τ is estimated as an inverse intercept of a linear regression plot of $\lambda(N)$ versus $1/N$. Since the value of A of Eq. (29) is not important to estimate τ, only the second half of the simulation data (i.e., $2 \times 10^5 < N < 4 \times 10^5$) was included in the calculations. Then, the diffusive tortuosity factor (defined in Eq. (18)) is illustrated in Fig. 6 as a function of cake volume fraction ϕ for the four different model structures.
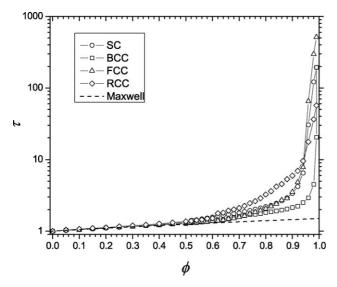

Fig. 5. RCC structure: dimensionless diffusion coefficient λ_{RCC} as a function of time step N.

Fig. 6. Diffusive tortuosity factor τ ($= D_0/D_h$) versus the volume fraction ϕ of SC, BCC, FCC, and RCC structures, and Maxwell's theoretical prediction [48].

Fig. 7. Inverse formation factor $1/f$ ($= \varepsilon/\tau$) versus the volume fraction ϕ of SC, BCC, FCC, and RCC structures, and Maxwell's theoretical prediction [48].

5.2.1. Structural indifference

In addition to the four structures used, Maxwell's theoretical equation [48,49], i.e.,

$$\tau = 1 + \frac{1}{2}\phi \tag{30}$$

is also plotted in Fig. 6. Neale and Nader [50] developed an identical expression to Eq. (30) by modeling a homogeneous, isotropic porous medium composed of spherical particles. In their model, a spherical cavity stands in a uniform porous medium and has an impermeable solid sphere at its center. The solid sphere radius is smaller than the cavity radius. Appropriate boundary conditions are applied to surfaces of the cavity and inner sphere. This geometrical simplification provides great physical insight into diffusive flow processes occurring within the homogeneous swarm of spherical particles. The particle swarm is, however, too simplified to characterize effects of porous medium structure on the diffusive processes. Nevertheless, Fig. 6 shows that the simulation results of the four different cake structures and the theoretical prediction for a homogeneous porous medium are agreeably superimposed onto each other as the volume fraction reaches as much as 0.5. For a low-volume fraction (i.e., high porosity) Maxwell's theory is reliably valid and surprisingly accurate, amplifying the structural indifference of the diffusive tortuosity factor. This indifference stems from (i) larger portion of void space than volume occupied by solid spheres, (ii) much smaller scale of the random walkers' mean free path compared to mono-dispersed sphere size, and (iii) 3D (instead of 2D) Euclidian space wherein the random walkers can easily find other routes to spatially diffuse in an entropic manner. The diffusive tortuosity factors of the four different structures in Fig. 6 deviate from Maxwell's theoretical prediction and become distinct from each other as the cake volume fraction exceeds 0.5 and further surpass the maximum packing ratios (i.e., 0.524, 0.680, 0.741, and 0.580 of SC, BCC, FCC, and RCC structures, respectively). In the complete span of the volume fraction, Maxwell's theory never outmatches but simply
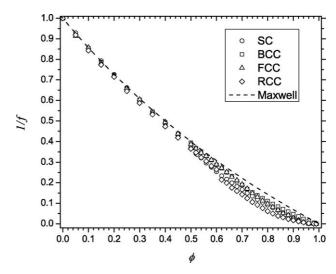
underlies the simulated tortuosity factors (especially for volume fraction greater than ∼0.5), re-emphasizing that the theory is cogent only for low-volume fractions.

5.2.2. Cake irregularity

In Fig. 6, the diffusive tortuosity factor of the RCC structure dominates near and above the cake volume fraction of 0.58, from which a particle can start overlapping with adjacent particles. As described above, this overlapping mimics cake compression based on the deformation of soft particles (i.e., microorganisms). A slight but noticeable jump of the RCC tortuosity factor near $\phi = 0.6$ indicates that particle overlapping introduces the random walkers to a geometrically different diffusion environment. The corresponding trend can be found in Fig. 7. Before the overlap, the diffusion is based on the tracers detouring around the particles to avoid geometrical obstruction. However, once the overlap is fully established, the tracers' diffusion will be similar to penetrating through irregularly established 3D pore channels. Although the overlap is common for all four structures, the RCC structure shows the superiority of its tortuosity factor in the volume fraction ranging from 0.6 to 0.9. In this light, the structural irregularity, expressed as random configuration of particle positions within the RCC cake layer, is considered here as a main cause of the highest tortuosity factor.

5.2.3. Periodic nesting

Comparison of the tortuosity factors of the three crystal structures (i.e., SC, BCC, and FCC) in Fig. 6 indicates that the BCC structure has a lower tortuosity factor than any other crystal structures for volume fraction greater than about 0.74. SC and FCC structures have very close tortuosity factors over the entire domain of volume fraction. This similarity of SC and FCC structures can be understood by visually scrutinizing Fig. 1. Unlike the SC and FCC structures, BCC has a particle at the center of the unit cell, so it appears to provide more winding paths with random walkers. However, the simulation contradictorily reveals that diffusion is less hindered in the BCC structure than

in the SC and FCC configurations. Note that composing spheres are positioned only at corners and/or surfaces of SC and FCC cells (shown in Fig. 1) and therefore render nested void spaces in their central regions. The BCC structure provides relatively more uniform porous medium than SC and FCC, which have a spatial periodicity with pairs of voided central nests and occupied particle bodies. In other words, spatial variation of the pore space is more significant in SC and FCC structures, resulting in higher tortuosity factors than that of the BCC structure. Tracer solutes will stay longer in locally nested void spaces, being reflected by partial surfaces of encompassing particles. It will take a certain amount of time for the tracers to escape from one nearby nest to another by passing through naturally generated transport tunnels among the equal-sized particles. It is further implied that hindered diffusion can be more serious in a polydispersed cake layer, where pore-size heterogeneity is ubiquitous in comparison to a monodispersed layer of the same volume fraction.

5.3. Inverse formation factor

The inverse formation factor, interpreted as the ratio of the diffusive flux in the cake layer to that in the bulk phase (free space), i.e.,

$$\frac{1}{f} = \frac{\varepsilon}{\tau} \tag{31}$$

is shown in Fig. 7 for the four cake structures and Maxwell's theory. Structural trends of the formation factor are very similar to those of the tortuosity factor. Remarkable indifference of cake structures reappears in the inverse formation factor where volume fraction is less than 0.5. The inverse formation factors of the three crystal structures are bounded by those of Maxwell's theory and RCC for volume fraction greater than 0.6. On the other hand, the unique effect of the BCC homogeneity does not noticeably emerge in Fig. 7, instead the three crystal structures provide similar inverse formation factors. Conversely, clear variation of the tortuosity factor with compressed cake structures is somehow suppressed by porosity ε in Eq. (31). The declining trend of the inverse formation factor with increasing volume fraction therefore stems from the diminishing presence of void spaces, including path tunnels among the nested local voids, which solutes can exist and diffuse in.

5.4. Dimensionless surface-to-volume ratio

Fig. 8 illustrates the dimensionless surface-to-volume ratio s_p (defined in Eq. (22)) as a function of volume fraction and structure for the four different models of porous media. Initial parts of λ (N) versus N (≤ 1000) curves shown in Figs. 2–5 were used to estimate s_p for each volume fraction. Each curve was fitted using a fourth-order polynomial series with respect to $\sqrt{N}$. The coefficient of the first-order term, i.e., $O(\sqrt{N})$, was used to calculate s_p.

As ϕ increases in a low-volume fraction region ($\phi < 0.5$), the volume of each constituent sphere increases monotonously so that a linear relationship between s_p and ϕ is established as shown in Fig. 8. The sphere-overlap occurring in a high-
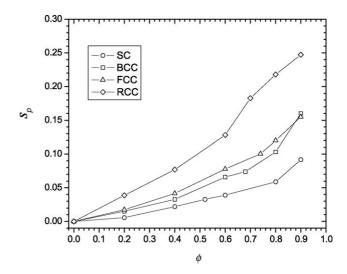

Fig. 8. Dimensionless surface-to-volume ratio s_p versus the volume fraction ϕ of SC, BCC, FCC, and RCC structures.

volume fraction region ($\phi > 0.5$) induces the nonlinearity of s_p with respect to ϕ, which implies much more curved pore surfaces, given a total pore volume. Fig. 8 also elucidates that RCC structure has the most surface area that can be seen by the random walkers while SC has the least, and BCC and FCC structures are similar to each other. In this light, the comparison between the structural similarities illustrated in Figs. 6 and 8 indicates that the surface-to-volume ratio is not solely sufficient to explain or predict the structural variation of the tortuosity factor.

5.5. Implications

5.5.1. Effect of solute size

In the current study, solute ions diffusing within the solid and soft cake layers composed of spherical particles (including solid colloids and deformable microorganisms) are considered as non-interacting tracers in the 3D pore spaces. Typical applications of the simulation results are colloidal and biofilm fouling during NF and RO processes that include the CEOP and CECP phenomenon [14,15]. Sizes of solute (salt) ions are usually a few orders of magnitude smaller than those of particles retained on the membrane surfaces.

While interactions between the solutes and the particle surfaces, i.e., solute–particle interactions, are negligible enough not to affect the solutes' random motions, the current simulation approach can provide a qualitative analysis of the diffusion of solutes whose sizes are less but comparable to the particle size. An effective particle radius can be considered as the real particle radius plus the solute radius. Then, the solutes can be treated as volumeless tracers diffusing in a new equivalent cake layer composed of the particles with the effective radius. Then, a corresponding tortuosity can be obtained by using a new effective volume fraction calculated with the effective radius.

5.5.2. Effect of solute–particle interactions

Any solute–particle interactions additionally hinder the solute diffusion on top of the geometrical obstruction due to the presence of the retained particles. If interactions are net attractive

and hence induce adsorption of solutes on particle surfaces, then solutes stay longer nearby and/or stick to the particle surfaces so that their random movements are subsequently hindered. If the solute–particle interactions are net repulsive, then the solute movements mostly occur away from particle surfaces, i.e., near a central zone of a local void (see Fig. 1). Solute diffusion under the repulsive interaction can be intuitively equivalent to the diffusion of tracers in a cake layer composed of particles of a bigger effective radius as described in the previous section. In other words, the effective radius is approximately equal to the real particle radius plus the force-range of the net repulsive interaction. In the presence of either the attractive or the repulsive interactions, therefore, the solute diffusion is more hindered with a specific cake structure so that the corresponding diffusive tortuosity factor must be higher than that of each structure shown in Fig. 6.

5.5.3. Effects on filtration performance

Based on the discussion above, further analyses can be conducted for membrane filtration performance. First, the structural indifference shows very similar formation factors for all four candidate structures when their volume fractions are less than ~0.5. This volume fraction range widely includes the particle CP layers before transition to solid-like cake layers. In this light, Maxwell's theoretical prediction is accurate enough to estimate the enhanced CP of tracer solutes due to the presence of the particle CP layer. Second, during the NF/RO filtration processes with biofilm fouling, the permeate flux decline may occur in different manners based on the structure of retained particles of a cake layer. Stochastic analysis of filtration experiments may be necessary because of the uncertainty of cake structures. Third, and more important, any effects of the finite solute-size, solute adsorption, and repulsive solute–particle interaction will additionally hinder the solute back-diffusion from the cake layer to the bulk phase and hence reduce the inverse formation factor. Regarding these aspects, flux prediction with the results from the current study will provide the maximum possible permeate flux based on the presumption of non-interacting, volumeless solute tracers and possibly overestimate the experimentally measured permeate flux. Nevertheless, the estimation of the maximum flux can contribute to effective designs of membrane separation systems and/or in-depth interpretations of filtration measurements.

Overall, the current study aims to qualitatively interpret experimental observations of the CEOP and CECP phenomena [14,15] and further provide more fundamental understanding of the filtration episodes. Novel experimental techniques can verify the current results and complement the simulation approach.

6. Conclusions

The diffusive tortuosity factors of solid and soft cake layers are successfully investigated using the Pearsonian random walk simulation method. For volume fractions less than ~0.5, Maxwell's theory [48], later confirmed by Neale and Nader [50], is valid and accurate, indicating that cake structure only negligibly affects the solute diffusion within the cake layer. For high volume fractions greater than ~0.5, including compressed cakes, different cake constructions do provide distinct effects on the diffusive transport of tracer solutes. The irregular colloidal cake layer does not cause any anomalous diffusion but renders the highest tortuosity factor while Maxwell's theory gives the lowest. Comparison of the tortuosity factors of the three different crystal structures indicates that if a cake layer has periodicity of local voids like SC and FCC structures, then tracer solutes are confined and stay longer in the local voids, and therefore their diffusion is more hindered. The cake irregularity and periodic nesting effects are somewhat less apparent in the inverse formation factor because the diminishing void volume suppresses solute diffusive flux in addition to the tortuousness of the cake layer. Our study infers that using Maxwell's expression will overestimate the permeate flux due to underestimates of solute concentration as well as osmotic pressure within the cake layer.

Nomenclature

BCC	body-centered cubic
C	solute number concentration within void space of cake layer
d_{max}	maximum pore diameter
d_{mean}	mean pore diameter
d_{min}	minimum pore diameter
$D(t)$	effective time-dependent diffusion coefficient
D_h	hindered diffusion coefficient in cake layer, D_0/τ
D_0	diffusion coefficient in bulk phase
f	formation factor
FCC	face-centered cubic
G	diffusion propagator
J	solute diffusive flux
$\bar{l}$	mean free path of random walkers
L'	length (or angle) factor
$\hat{\mathbf{n}}$	unit vector normal to the particle surface
N	number of time steps
N_p	number of random walkers
$\mathbf{r}$	random walker position at time t
$\mathbf{r}'$	random walker position at time $t = 0$
$\mathbf{R}$	dimensionless tracer coordinate scaled with $\bar{l}$
$\mathbf{R}'$	dimensionless tracer coordinate at time $t = 0$
RCC	random colloidal cake
s_p	dimensionless surface-to-volume ratio
S	total pore surface area
S'	shape factor
SC	simple cubic

t	time
V_p	volume of void space
y	vertical coordinate normal to the membrane surface

Greek symbols

ε	porosity of cake layer
λ	dimensionless effective time-dependent diffusion coefficient in the cake layer of Eq. (10)
λ_{free}	dimensionless effective time-dependent diffusion coefficient in the free space
θ	diffusive tortuosity
τ	diffusive tortuosity factor

References

[1] C.A. Romero, R.H. Davis, Global model of crossflow microfiltration based on hydrodynamic particle diffusion, J. Membr. Sci. 39 (1988) 157.

[2] C.A. Romero, R.H. Davis, Transient model of crossflow microfiltration, Chem. Eng. Sci. 45 (1990) 13.

[3] C.A. Romero, R.H. Davis, Experimental verification of the shear-induced hydrodynamic diffusion model of crossflow microfiltration, J. Membr. Sci. 62 (1991) 249.

[4] L.F. Song, M. Elimelech, Theory of concentration polarization crossflow filtration, J. Chem. Soc. Faraday Trans. 91 (1995) 3389.

[5] S. Hong, R.S. Faibish, M. Elimelech, Kinetics of permeate flux decline in crossflow membrane filtration of colloidal suspensions, J. Colloid Interf. Sci. 196 (1997) 267.

[6] L. Song, Flux decline in crossflow microfiltration and ultrafiltration: mechanisms and modeling of membrane fouling, J. Membr. Sci. 139 (1998) 183.

[7] R.S. Faibish, M. Elimelech, Y. Cohen, Effect of interparticle electrostatic double layer interactions on permeate flux decline in crossflow membrane filtration of colloidal suspensions: an experimental investigation, J. Colloid Interf. Sci. 204 (1998) 77.

[8] S. Bhattacharjee, A.S. Kim, M. Elimelech, Concentration polarization of interacting solute particles in cross-flow membrane filtration, J. Colloid Interf. Sci. 212 (1999) 81.

[9] A.S. Kim, E.M.V. Hoek, Cake structure in dead-end membrane filtration: Monte Carlo simulation, Environ. Eng. Sci. 19 (2002) 373.

[10] W.R. Bowen, F. Jenner, Dynamic ultrafiltration model for charged colloidal dispersions: a Wigner-Seitz cell approach, Chem. Eng. Sci. 50 (1995) 1707.

[11] G.Y. Onoda, E.G. Liniger, Random loose packing of uniform spheres and the dilantancy onset, Phys. Rev. Lett. 64 (1990) 2727.

[12] W. Soppe, Computer simulation of random packings of hard spheres, Powder Tech. 62 (1990) 189.

[13] G.T. Nolan, P.E. Kavanagh, Computer simulation of random packing of hard spheres, Powder Tech. 72 (1992) 149.

[14] E.M.V. Hoek, A.S. Kim, M. Elimelech, Influence of crossflow membrane filter geometry and shear rate on colloidal fouling in reverse osmosis and nanofiltration separations, Environ. Eng. Sci. 19 (2002) 357.

[15] E.M.V. Hoek, M. Elimelech, Cake-enhanced concentration polarization: a new fouling mechanism for salt-rejecting membranes, Environ. Sci. Technol. 37 (2003) 5581.

[16] D.G. Allison, I.W. Sutherland, A staining technique for attached bacteria and its correlation to extracellular carbohydrate production, J. Microbiol. Methods 2 (1984) 93.

[17] J.W. Costerton, K.J. Cheng, G.G. Geesey, T.I. Ladd, J.C. Nickel, M. Dasgupta, T.J. Marrie, Bacterial biofilms in nature and disease, Ann. Rev. Microbiol. 41 (1987) 435.

[18] H.F. Ridgway, A. Kelly, C. Justice, B.H. Olson, Microbial fouling of reverse-osmosis membranes used in advanced wastewater treatment technology: chemical, bacteriological, and ultrastructural analyses, Appl. Environ. Microbiol. 45 (1983) 1066.

[19] G.G. Geesey, M.W. Stupy, P.J. Bremer, The dynamics of biofilms, Int. Biodeter. Biodegr. 30 (1992) 135.

[20] J.D. Bryers, Bacterial biofilms, Curr. Opin. Biotechnol. 4 (1993) 197.

[21] P.A. Suci, M.W. Mittelman, F.P. Yu, G.G. Geesey, Investigation of ciprofloxacin penetration into *Pseudomonas aeruginosa* biofilms, Antimicrob. Agents Chemother. 38 (1994) 2125.

[22] D.C. Brandt, G.F. Leitner, W.E. Leitner, Reverse osmosis membranes state of the art, in: A. Amjad (Ed.), Reverse Osmosis: Membrane Technology, Water Chemistry, and Industrial Applications, Van Nostrand Reinhold, New York, 1993, p. 1.

[23] H.F. Ridgway, C.A. Justice, C. Whittaker, D.G. Argo, B.H. Olson, Biofilm fouling of RO membranes: its nature and effect on treatment of water for reuse, J. Am. Water Works Assoc. 76 (1984) 94.

[24] J.W. Costerton, Z. Lewandowski, D. Debeer, D. Caldwell, D. Korber, G. James, Biofilms, the customized microniche, J. Bacteriol. 176 (1994) 2137.

[25] D.N. Petsev, V.M. Starov, I.B. Ivanov, Concentrated dispersions of charged colloidal particles: sedimentation, ultrafiltration and diffusion, Colloid Surf. A 81 (1993) 65.

[26] C. Kittel, Introduction to Solid-state Physics, John Wiley and Sons Inc., New York, 1995.

[27] J. Martins, K.R. Naqvi, E. Melo, Kinetics of two-dimensional diffusion-controlled reactions: a Monte Carlo simulation of hard-disk reactants undergoing a Pearson-type random walk, J. Phys. Chem. B 104 (2000) 4986.

[28] W.J. Ullman, R.C. Aller, Diffusion coefficients in nearshore marine sediments, Limnol. Oceanogr. 27 (1982) 552.

[29] J.-P.R.A. Sweets, C.A. Kelly, J.W.M. Rudd, R. Hesslein, T.E. Cappenberg, Similarity of whole-sediment molecular diffusion coefficients in freshwater sediments of low and high porosity, Limonol. Oceanogr. 36 (1991) 335.

[30] N. Iversen, B.B. Jorgensen, Diffusion coefficient of sulfate and methane in marine sediments: influence of porosity, Geochem. Cosmochim. Acta 57 (1993) 571.

[31] B.P. Boudreau, The diffusive tortuosity of fine-grained unlithified sediments, Geochim. Cosmochim. Acta 60 (1996) 3139.

[32] P.C. Carman, Fluid flow through a granular bed, Trans. Inst. Chem. Eng. 15 (1937) 150.

[33] M.D. Krom, R.A. Berner, The diffusion coefficients of sulfate, ammonium, and phosphate ions in anoxic marine sediments, Limnol. Oceangr. 25 (1980) 327.

[34] K.-J. Dunn, D.J. Bergman, Self diffusion of nuclear spins in a porous medium with a periodic microstructure, J. Chem. Phys. 102 (1995) 3041.

[35] U. Hizi, D.J. Bergman, Molecular diffusion in periodic porous media, J. Appl. Phys. 87 (2000) 1704.

[36] P.P. Mitra, P.N. Sen, L.M. Schwartz, Short-time behavior of the diffusion coefficient as a geometrical probe of porous media, Phys. Rev. B 47 (1993) 8565–8574.

[37] L.L. Latour, P.P. Mitra, R.L. Kleinberg, C.H. Sotak, Time-dependent diffusion coefficient of fluids in porous media as a probe of surface-to-volume ratio, J. Magn. Reson. Ser. A 101 (1993) 342–346.

[38] N.S. Pabitra, Time-dependent diffusion coefficient as a probe of geometry, Concepts Magn. Reson. Part A 23A (2004) 1–21.

[39] S. Trinh, P. Arce, B.R. Locke, Effective diffusivities of point-like molecules in isotropic porous media by Monte Carlo simulation, Transport Porous Media 38 (2000) 241–259.

[40] V. Pham, M.W. Deem, Direct numerical observation of anomalous diffusion in random media, J. Phys. A: Math. Gen. 31 (1998) 7235.

[41] W. Gropp, E. Lusk, A. Skjelum, Using MPI: Portable Parallel Programming with the Message-passing Interface, The MIT Press, Cambridge, Massachusetts, 1997.

[42] Y. Gefen, A. Aharony, Anomalous diffusion on percolating clusters, Phys. Rev. Lett. 50 (1983) 77.

[43] J.-P. Bouchaud, A. Georges, Anomalous diffusion in disordered media: statistical mechanisms, models and physical applications, Phys. Rep. 195 (1990) 127.

[44] F.H. Stillinger, T.A. Weber, Hidden structure in liquids, Phys. Rev. A 25 (1982) 978.

[45] M.P. Allen, D.J. Tildesley, Computer Simulation of Liquids, Oxford Science Publications, Oxford, UK, 1987.

[46] G.S. Armatas, C.E. Salmas, M. Louloudi, G.P. Androutsopoulos, P.J. Pomonis, Relationships among pore size, connectivity, dimensionality of capillary condensation, and pore structure tortuosity of functionalized mesoporous silica, Langmuir 19 (2003) 3128–3136.

[47] C.N. Satterfield, Mass Transfer in Heterogeneous Catalysis, MIT Press, Cambridge, MA, 1970.

[48] J.C. Maxwell, Treatise on Electricity and Magnetism, Dover Publications, Inc., New York, 1981.

[49] E.L. Cussler, Diffusion: Mass Transfer in Fluid Systems, Cambridge University Press, New York, 1984.

[50] G. Neale, W.K. Nader, Prediction of transport processes within porous media: diffusive flow processes within an homogeneous swarm of spherical particles, AIChE J. 19 (1973) 112.